Adaptive Model-Free Deadbeat Predictive Current Control for Linear Permanent Magnet Synchronous Motor Based on Immune Algorithm

Yanqing Zhang, *Member, IEEE*, Hongtao Yuan, Zhonggang Yin, *Member, IEEE*, and Cong Bai

***Abstract*—The model free deadbeat predictive current control (MFDPCC) for linear permanent magnet synchronous motor (LPMSM) drive system is emerging as a promising method due to its straightforward structure and strong parameter robustness. However, the conventional MFDPCC controller with the fixed gain leads to a contradiction between the dynamic and steady-state performance. To overcome this limitation, an adaptive MFDPCC based on immune algorithm is proposed in this article. First, the impact of the parameters mismatch on traditional DPCC is analyzed. Then, an ultralocal model, known as a typical branch of model free control, is developed to replace the conventional LPMSM model. For the ultralocal model with a typical fixed gain, the control performance is analyzed in detail, and it points out that there exits the contradiction between the dynamic and steady-state performance. Thus, to effectively balance the conflict, the immune algorithm is introduced to optimize the fixed parameter adaptively. Finally, the experimental test is carried out on a 0.9-kW LPMSM test bench, and the experimental results verify the effectiveness of the proposed method.**

***Index Terms*—Deadbeat predictive current control (DPCC), immune algorithm (IA), linear permanent magnet synchronous motor (LPMSM), model free control (MFC).**

I. Introduction

THE linear motor has received increasing attention in recent years. Unlike traditional rotary type motors that rely on reduction gears and ball screws, linear motors directly provide thrust to loads, eliminating the need for mechanical transmission [1]. Furthermore, this direct action gives the mover more motion freedom than moving coil motors and avoids cable-related restrictions [2]. Since it is able to perform the linear motion directly without the need for any intermediate conversion mechanism, thereby providing several advantages, such as a simplified structure, dependable performance, minimal mechanical loss, high environmental adaptability and low noise [3]. As a key type of linear motors, linear permanent magnet synchronous motor (LPMSM) has drawn widespread attention from academic and industrial circles [4]. Currently, LPMSM has been widely used in high-end manufacturing areas such as aerospace, semiconductor fabrication, high-speed logistics, and precision machining [5].

As known, the current loop control strategy is of great significance for achieving high performance control of LPMSM. To enhance the current control performance, various current control strategies have been explored. Among them, deadbeat current predictive control (DPCC) has grown into a highly attractive alternative strategy due to its rapid dynamic response, low computational demands and excellent steady-state tracking performance [6]. However, it is known that the precise control of DPCC is highly sensitive to motor model accuracy in practical implementations [7]. In practical operations, the motor parameters including inductance, resistance and other parameters vary with temperature and operating conditions, leading to the parameters mismatch and then resulting in increased current and torque ripple [8]. To enhance the system robust performance against such parameters variation, numerous different approaches have been developed, which can be generally categorized into three groups, i.e., the parameters identification [9], the disturbance observer [10], and model free control (MFC) [11].

The first group is the parameters identification method, which is regarded as a direct solution to solve the problem of parameters mismatch. The identification algorithm estimates motor parameters online and updates the motor model in real-time to cope with the parameters mismatch problem. Nowadays, many online parameters identification methods are available for estimating the motor parameters, such as gradient descent [12], extended Kalman filter [13] and model reference adaptive systems (MRAS) [14]. In [15], an enhanced DPCC method is presented, in which the permanent magnet flux and stator inductance are identified online based on MRAS. However, it is noticeable that the dead-time voltage needs to be manually compensated before the identification. In [16], a parameter identification method is presented that utilizes high-frequency (HF) signals injected into both d- and q-axes. This method effectively addresses inverter nonlinearities and mitigates the effects of HF signals on parameter identification. For the parameter identification methods, they effectively address the issue of parameters mismatch during dynamic operation. Nevertheless, the identification process also

Received 31 December 2024; revised 12 March 2025; accepted 16 April 2025. Date of publication 22 April 2025; date of current version 30 June 2025. This work was supported in part by the National Natural Science Foundation of China under Grant 52107206, Grant 52177194, and Grant 52407221, in part by the China Postdoctoral Science Foundation under Grant 2020M683524, and in part by the Nature Science Basic Research Plan in Shaanxi Province under Grant 2024JC-YBQN-0510. Recommended for publication by Associate Editor M. Hartmann. *(Corresponding author: Zhonggang Yin.)*

The authors are with the School of Electrical Engineering, Xi'an University of Technology, Xi'an 710048, China (e-mail: zhangyanqing@xaut.edu.cn; 2221921141@stu.xaut.edu.cn; zhgyin@xaut.edu.cn; baicong@xaut.edu.cn).

Color versions of one or more figures in this article are available at https://doi.org/10.1109/TPEL.2025.3563247.

Digital Object Identifier 10.1109/TPEL.2025.3563247

increases system complexity, and the precision of parameter identification directly impacts the control performance of the drive system [17].

The second group to address the parameters mismatch problem is to design a disturbance observer. This method observes and compensates for disturbances caused by parameter mismatch and unmodeled factors in the drive system. In [18], a discrete Luenberger observer (LO) is presented for estimating the stator current and disturbance, achieving rapid and error-free current tracking performance despite parameter mismatches. In [19], a modified discrete-time sliding mode disturbance observer with updated coefficients is presented to address parameter dependence. In [20], a robust DPCC based on an improved discrete-time resonant extended state observer is presented to achieve static-errorless tracking accuracy while maintaining high performance control. In [21], a modified DPCC using an iterative sliding mode observer is presented to enhance the accuracy of current control. The presented method not only reduces current harmonics and the tracking error, but also substantially improves the system's robustness. However, it is known that most disturbance observer methods depend on an accurate motor model [22]. Additionally, some disturbance observers are complex to design and require substantial parameter adjustment efforts.

The third group, MFC, is known as a strong and promising robust method that minimizes reliance on motor parameters, requiring only system input and output [23]. In [24], for PMSM, an enhanced model free active disturbance rejection DPCC based on data-driven is presented to address the challenge of parameters mismatch. In [25], a model free DPCC using the ultralocal model is presented, which outperforms traditional DPCC in robustness and steady-state performance. Zhang et al. [26] present an enhanced MFC with an ultralocal model, eliminating the need for motor parameters, reducing computational effort, and delivering superior performance in current harmonics suppression, tracking error minimization, and dynamic overshoot mitigation. In [27], for servo systems, an advanced ultralocal MFC strategy is presented, which exhibits superior performance in response tracking and disturbance rejection. In [28], an adaptive ultralocalized time-series based model-free predictive current control is developed. The method simplifies the realization in CCS-type controllers through the ultralocalization of intricate discrete-time transfer functions. A model-free predictive control strategy based on a sinusoidal generalized universal model is presented in [29], in which the accuracy of the model is enhanced by the incorporation of past data to better reflect the motion characteristics of the plant. For the MFC method, the ultralocal model is typically designed to replace the conventional motor model. However, for the conventional ultralocal model with the fixed gain, there exits the contradiction between the dynamic and steady-state performance, and it is difficult to achieve the balance between the dynamic and steady-state performance simultaneously.

In this article, an adaptive MFDPCC based on immune algorithm (AMFDPCC-IA), is proposed to address the issue of performance degradation in conventional MFDPCC caused by the typical fixed controller gain. The immune algorithm (IA), known as an emerging intelligent algorithm developed based on immunology theory, is introduced to dynamically adjust the controller gain. As an adaptive global optimization technique with strong learning capability and adaptability, the IA has been widely applied in function optimization, model recognition, machine learning, and other research fields [30]. In this article, the IA is introduced for its simplicity in implementation and remarkable effectiveness in dynamically adjusting the parameters of the model-free deadbeat predictive current control with increasing an acceptable computational complexity [31]. Additionally, noise data can be effectively filtered by the antibody selection mechanism of the IA, thereby demonstrating strong noise resistance [32]. Furthermore, the IA offers significant improvements in adaptability and robustness, particularly in scenarios where system dynamics are uncertain or time-varying [33].

An DPCC controller is typically constructed in this article, and the impact of the parameters mismatch on DPCC is analyzed in detail. To eliminate the parameter dependency, this article designs the MFDPCC, an integration of the MFC and DPCC, with the linear extended state observer (LESO) employed for unknown part estimation. On this basis, the impact of the controller gain on both the system's dynamic and steady-state performance is analyzed in detail, and it points out that there exits the contradiction between the dynamic and steady-state performance. To address this issue, the IA is introduced to dynamically adjust the controller gain. The experimental results demonstrate that in comparison to the conventional MFDPCC, the proposed AMFDPCC-IA exhibits the improved dynamic and steady-state performance.

II. Deadbeat Predictive Current Control

A. Mathematical Model of LPMSM

The dq-axis stator voltage model of LPMSM is described as

$$\begin{cases} u_d = L_d \frac{di_d}{dt} + R_s i_d - \frac{\pi v}{\tau} L_d i_d - \frac{\pi v}{\tau} \psi_f \\ u_q = L_q \frac{di_q}{dt} + R_s i_q + \frac{\pi v}{\tau} L_q i_q \end{cases} \tag{1}$$

where u_d and u_q are the stator voltages of d- and q-axis, i_d and i_q are the stator current of d- and q-axis. R_s is the stator resistance, τ is pole pitch, and v is the velocity of the mover. In the surface-mounted LPMSM, the d-axis inductance and q-axis inductance are equal, i.e., $L_d = L_q = L_s$. ψ_f is the permanent magnet flux linkage.

According to (1), the current state equation of the motor can be obtained as

$$\begin{cases} \frac{di_d}{dt} = -\frac{R_s}{L_d} i_d + \frac{u_d}{L_d} + \frac{\pi L_q}{\tau L_d} v i_q \\ \frac{di_q}{dt} = -\frac{R_s}{L_q} i_d + \frac{u_d}{L_q} - \frac{\pi L_d}{\tau L_q} v i_d - \frac{\pi \psi_f}{\tau L_q} v \end{cases}. \tag{2}$$

The electromagnetic thrust equation can be expressed as

$$F_e = p_n \frac{3\pi}{2\tau} \left[\psi_f i_q + (L_d - L_q) i_d i_q \right] = p_n \frac{3\pi}{2\tau} \psi_f i_q \tag{3}$$

where F_e is the electromagnetic thrust and p_n is the number of pole pairs.

The mechanical dynamic equation of LPMSM can be expressed as

$$m\frac{dv}{dt} = F_e - F_l - Bv \tag{4}$$

where m is the mover mass, F_l is the load force, and B is the viscous fiction coefficient.

B. Deadbeat Predictive Current Control

It is known that the DPCC algorithm consists of two key components: current prediction and reference voltage calculation. According to the current sampling value of the motor, the predicted current for the next control period is calculated based on (2). On the basis of obtaining the predicted current, the reference voltage for the next control period is calculated through the discrete voltage equation. By discretizing (2), the current prediction equation of LPMSM can be derived as

$$\begin{cases} i_d(k+1) = \left(1 - \frac{R_s}{L_d}T_s\right) i_d(k) + \frac{T_s}{L_d}u_d(k) \\ \qquad\qquad + \frac{T_s L_q}{L_d}\frac{\pi}{\tau}v(k)i_q(k) \\ i_q(k+1) = \left(1 - \frac{R_s}{L_q}T_s\right) i_q(k) + \frac{T_s}{L_q}u_q(k) \\ \qquad\qquad - \frac{T_s L_d}{L_q}\frac{\pi}{\tau}v(k)i_d(k) - \frac{T_s\psi_f}{L_q}\frac{\pi}{\tau}v(k) \end{cases} \tag{5}$$

where T_s is the sampling time. $i_d(k+1)$ and $i_q(k+1)$ are the predicted values of dq-axis currents for the $(k+1)$th control period. $i_d(k)$ and $i_q(k)$ are the sampled values of dq-axis currents for the kth control period. $\nu(k)$ is the velocity for the kth control period. $u_d(k)$ and $u_q(k)$ are the dq-axis reference voltages for the $(k+1)$th control period. By discretizing (1), the reference voltage can be calculated as

$$\begin{cases} u_d^*(k+1) = R_s i_d(k+1) + \frac{L_d}{T_s}[i_d^*(k+2) - i_d(k+1)] \\ \qquad\qquad - L_q\frac{\pi}{\tau}v(k)i_q(k+1) \\ u_q^*(k+1) = R_s i_q(k+1) + \frac{L_q}{T_s}[i_q^*(k+2) - i_q(k+1)] \\ \qquad\qquad + \frac{\pi}{\tau}v(k)\left[L_d i_q(k+1) + \psi_f\right] \end{cases} \tag{6}$$

where $i_d^*(k+2)$ and $i_q^*(k+2)$ are the d-axis and q-axis reference currents for the $(k+2)$th control period. $u_d^*(k+1)$ and $u_q^*(k+1)$ are d-axis and q-axis reference voltages for the $(k+1)$th control period. During the operation process, once the parameters mismatch occurs, the current prediction equation shown in (5) will transformed into

$$\begin{cases} i'_d(k+1) = \left(1 - \frac{R_s}{L_d}T_s\right) i_d(k) + \frac{T_s}{L_d}u_d(k) \\ \qquad\qquad + \frac{T_s L_q}{L_d}\frac{\pi}{\tau}v(k)i_q(k) + \Delta\delta_d \\ i'_q(k+1) = \left(1 - \frac{R_s}{L_q}T_s\right) i_q(k) + \frac{T_s}{L_q}u_q(k) \\ \qquad\qquad - \frac{T_s L_d}{L_q}\frac{\pi}{\tau}v(k)i_d(k) - \frac{T_s\psi_f}{L_q}\frac{\pi}{\tau}v(k) + \Delta\delta_q \end{cases} \tag{7}$$

where $\Delta\delta_d$ and $\Delta\delta_q$ are the deviations due to the parameters mismatch, which can be described as

$$\begin{aligned} \Delta\delta_d = & -\frac{(R_s\Delta L_d - \Delta R_s L_d)}{L_d\left(L_d + \Delta L_d\right)}T_s i_d(k) \\ & + \frac{\Delta L_d}{L_d\left(L_d + \Delta L_d\right)}T_s u_d(k) \\ & + \frac{T_s\left(L_q\Delta L_d - L_q\Delta L_d\right)}{L_d\left(L_d + \Delta L_d\right)}\frac{\pi}{\tau}v(k)i_q(k) \\ \Delta\delta_q = & -\frac{(R_s\Delta L_q - \Delta R_s L_q)}{L_q\left(L_q + \Delta L_q\right)}T_s i_q(k) \\ & + \frac{\Delta L_q}{L_q\left(L_q + \Delta L_q\right)}T_s u_q(k) \\ & - \frac{T_s\left(L_d\Delta L_q - L_q\Delta L_d\right)}{L_d\left(L_d + \Delta L_d\right)}\frac{\pi}{\tau}v(k)i_q(k) \\ & - \frac{T_s\left(\psi_f\Delta L_q - \Delta\psi_f L_q\right)}{L_q\left(L_q + \Delta L_q\right)}\frac{\pi}{\tau}v(k)i_q(k) \end{aligned}$$

where ΔR_s, ΔL_d, ΔL_q, and $\Delta\psi_f$ represent the differences between the actual parameters and the parameters used in the controller.

Based on (6) and (7), it can be concluded that the control performance of DPCC is significantly influenced by the precision of the parameters. Once the parameters mismatch occurs, both the current ripple and torque ripple become more severe, and the control performance will decrease accordingly [34].

III. Model Free Deadbeat Predictive Current Control

A. Model Free Deadbeat Predictive Current Control

To enhance the parameter robustness of DPCC, the ultralocal model, known as a typical and effective MFC method, is formulated to replace the conventional LPMSM model, which can be described as [35]

$$\dot{y} = \alpha u + F \tag{8}$$

where u and y are the input and output of the system, and α is the gain that needs to be designed. F represents the unknown part of the ultralocal model, which includes the modeled part and the perturbed part.

To reduce the dependence of DPCC on the precision of the LPMSM model, an ultralocal model is established based on (2) and (8), which is shown as

$$\begin{cases} \frac{di_d}{dt} = \alpha u_d + F_d \\ \frac{di_q}{dt} = \alpha u_q + F_q \end{cases}. \tag{9}$$

According to (9), the discrete-time form of the predictive LPMSM model can be described as

$$\begin{cases} i_d(k+1) = i_d(k) + T_s(F_d(k) + \alpha u_d(k)) \\ i_q(k+1) = i_q(k) + T_s(F_q(k) + \alpha u_q(k)) \end{cases} \tag{10}$$

where α is the gain of the ultralocal model, F_d and F_q are assumed to be the unknown part of the plant. In this article, F_d and F_q are estimated by a typical LESO, which can be expressed as

$$\begin{cases} e_{dq} = z_1 - i_{dq} \\ \dot{z}_1 = z_2 + \alpha u_{dq} - \beta_1 e_{dq} \\ \dot{z}_2 = -\beta_2 e_{dq} \end{cases} \tag{11}$$

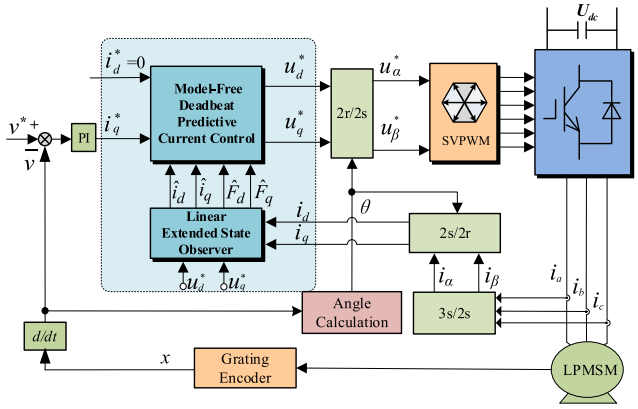

Fig. 1. Block diagram of LPMSM drive system based on MFDPCC.

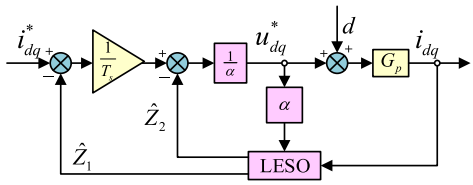

Fig. 2. Block diagram of MFDPCC.

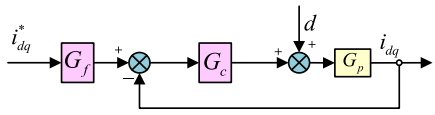

Fig. 3. Transformed block diagram of MFDPCC.

where z_1 and z_2 are the estimation of i_{dq} and F_{dq}, β_1 and β_2 are the error feedback coefficients of LESO.

The forward Euler discretization method is used to discretize (11). The discrete state space function can be derived as

$$\begin{cases} e_{dq}(k) = \hat{i}_{dq}(k) - i_{dq}(k) \\ \hat{i}_{dq}(k+1) = \hat{i}_{dq}(k) + T_s\left(\hat{F}_{dq}(k) + \alpha u_{dq}(k) - T_s\beta_1 e_{dq}(k)\right) \\ \hat{F}_{dq_s}(k+1) = \hat{F}_{dq}(k) - T_s\beta_2 e_{dq}(k) \end{cases} \tag{12}$$

where $\hat{i}_{dq}$ and $\hat{F}_{dq}$ are the estimated values of i_{dq} and F_{dq}.

According to (10) and (12), the reference voltage can be derived as

$$u^*_{dq}(k+1) = \frac{-\hat{F}_{dq}(k+1)T_s + i^*_{dq}(k+2) - \hat{i}_{dq}(k+1)}{\alpha T_s}. \tag{13}$$

Fig. 1 shows the block diagram of MFDPCC-based LPMSM drive system. The LPMSM control system comprises speed and current control loops, in which MFDPCC is designed in the current loop. The ultralocal model is used for current prediction, in which the unknown part is estimated by a typical LESO. On this foundation, the reference voltage, calculated by (13), is subsequently provided to the SVPWM module to generate the switching signal for the inverter.

B. Performance Analysis of Model Free Deadbeat Predictive Current Control

According to (11), the transfer function of LESO can be represented as

$$\begin{bmatrix} z_1(s) \\ z_2(s) \end{bmatrix} = \begin{bmatrix} \frac{\alpha s}{s^2+\beta_s s+\beta_2} & \frac{\alpha s}{s^2+\beta_s s+\beta_2} \\ \frac{-\beta_2\alpha}{s^2+\beta_s s+\beta_2} & \frac{-\beta_2 s}{s^2+\beta_s s+\beta_2} \end{bmatrix} \begin{bmatrix} u(s) \\ y(s) \end{bmatrix} \tag{14}$$

where $z_1(s)$ is the transfer function of the estimated dq-axis current, $z_2(s)$ is the transfer function of the estimated dq-axis disturbance. β_1 and β_2 are the gain coefficients of LESO. ω_0 is the bandwidth of the LESO.

In order to facilitate analysis, the control block diagram shown in Fig. 2 is constructed based on (11) and (13), in which d is the external unknown disturbance of the system.

The state equation of the block diagram shown in Fig. 2 can be described as

$$\begin{cases} \dot{\hat{Z}} = (A - LC)\hat{Z} + Bu + Ly \\ u = K(R - \hat{Z}) \end{cases} \tag{15}$$

where $Z = [Z_1\ Z_2]^T$, $A = \begin{bmatrix} 0 & 1 \\ 0 & 0 \end{bmatrix}$, $B = \begin{bmatrix} \alpha & 0 \end{bmatrix}^T$, $y = \begin{bmatrix} i_{dq} & 0 \end{bmatrix}^T$, $L = \begin{bmatrix} \beta_1 & \beta_2 \end{bmatrix}^T$, $C = \begin{bmatrix} 1 & 0 \end{bmatrix}$, $R = \begin{bmatrix} i^*_{dq} & 0 \end{bmatrix}^T$, $K = \begin{bmatrix} \frac{1}{\alpha T_s} & \frac{1}{\alpha} \end{bmatrix}$, $u = u^*_{dq}$. G_p is the transfer function of the motor current equation corresponding to dq-axis.

To facilitate the performance analysis of the controller, by integrating (14) and (15), the block diagram illustrated in Fig. 2 can be transformed into the configuration depicted in Fig. 3, in which G_f and G_c are the transfer functions obtained after the equivalent transformation of MFDPCC.

The transfer functions of each component depicted in Fig. 3 can be expressed as

$$G_p(s) = \frac{1}{R_s + L_{dq}s} \tag{16}$$

$$G_c(s) = \frac{s^2 + (T_s\beta_2 + \beta_1)s + k_p\beta_2}{T_s\alpha s(s + \beta_1)} \tag{17}$$

$$G_f(s) = \frac{\left(s + \frac{\beta_1}{2}\right)^2}{s^2 + (\beta_2 + k_p\beta_1)T_s s + \beta_2}. \tag{18}$$

The closed-loop transfer function of the current loop can be derived as

$$G_{YR}(s) = \frac{(s^2 + \beta_1 s + \beta_2)}{(T_s\alpha + G_p k_p)s^2 + (T_s\alpha\beta_1 + T_s G_p\beta_2 + G_p\beta_1)s + T_s G_p\beta_2} \tag{19}$$

$$G_{YD}(s) = \frac{T_s(G_p\alpha s^2 + G_p\alpha\beta_1 s)}{T_s(\alpha + G_p k_p)s^2 + T_s(\beta_1\alpha + G_p\beta_2 + G_p\beta_1)s + G_p k_p\beta_2}. \tag{20}$$

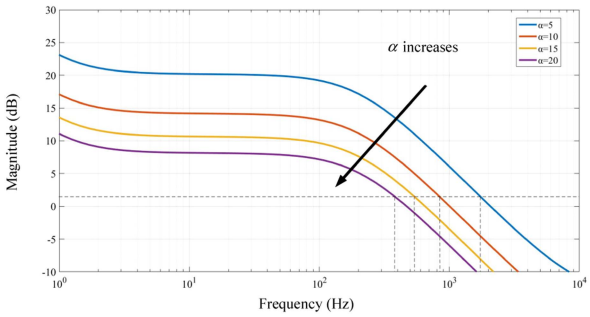

Fig. 4. Amplitude-frequency curve of $G_c(s)$.

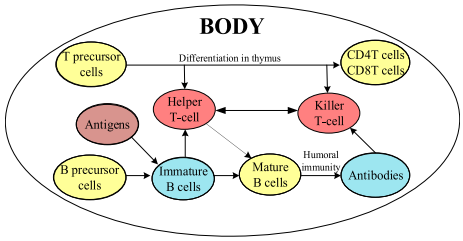

Fig. 5. Biological immune system illustration.

This article primarily investigates the impact of parameters on the controller, the performance analysis of MFDPCC can be divided into two aspects, i.e., the steady-state performance and the dynamic performance.

First, the steady-state performance analysis is conducted. When the input signal is a step response, the system's steady-state error can be expressed as

$$e_{ss} = \lim_{s\to 0} sR(s)G_{YR}(s) = \frac{1}{T_s\alpha}. \tag{21}$$

By analyzing (21), it is evident that an excessively small value will result in a significant error within the system. Consequently, a larger value of α leads to a reduced steady-state error.

On the other hand, it is known that there is no intermediate transmission mechanism between the linear motor and the load, which makes the linear motor more vulnerable to external disturbances. When the system is subjected to a low-frequency disturbance signal, since the frequency of the disturbance signal approaches 0, the Laplace operator s also approaches 0 based on the equivalence $s = j\omega$, then (20) will be approximated as

$$\begin{aligned} G_{YD}(s) = & \\ & \frac{T_s(G_p\alpha s + G_p\alpha\beta_1)}{(T_s\alpha + G_p)s^2 + T_s(\beta_1\alpha + G_p\beta_2 + G_p\beta_1)s + G_p\beta_2}s\Big|_{s\to 0} \\ & \approx \frac{T_sG_p\alpha\beta_1}{G_p\beta_2}s = \frac{2T_s\alpha}{\omega_0}s. \end{aligned} \tag{22}$$

Based on (22), it is evident that as the value of α increases, the influence of disturbances on the system becomes more intensified.

Combined with the results of steady-state analysis, it is evident that there exists a paradox, i.e., a higher value of α enhances the steady-state performance of the system. However, an excessively large α amplifies the impact of perturbations on the system at the same time.

For the analysis of $G_c(s)$ shown in Fig. 4, when β_1 and β_2 are kept unchanged, to achieve the balance between response speed and noise suppression, the ω_0 of the LESO is configured to 100 rad/s, with $\beta_1 = 2\omega_0$ and $\beta_2 = \omega_0^2$. The amplitude-frequency curve by adjusting the value of α can be obtained, which is shown in Fig. 4.

According to the amplitude-frequency curve shown in Fig. 4, it can be seen that as α increases continuously, the cutoff frequency of $G_c(s)$ consistently decreases, which indicates that an increase of α results in a degradation of the system's dynamic performance.

Through the analysis of both steady-state and dynamic performance of the system, it is evident that there exists a contradiction between the steady-state performance and dynamic performance. In a word, if the gain α is designed as a fixed value, just like what conventional MFDPCC does, it is difficult to achieve a good comprehensive effect between the steady-state performance and dynamic performance of the drive system.

IV. Proposed Adaptive Model Free Deadbeat Predictive Current Control With Immune Algorithm

In this article, the IA, developed from the biological immune system, is designed to dynamically adjust the gain α and then enhance the system performance.

A. Principle of the Biological Immune System

The IA is an adaptive global optimization technique inspired by natural selection and genetic principles. It leverages the biological immune system's learning and memory capabilities to solve optimization problems. As illustrated in Fig. 5, the biological immune system defends against foreign entities like bacteria and viruses through two main immunity types: humoral and cell-mediated. Key players include B-cells and T-cells, which mature in the bone marrow and thymus, respectively. Upon pathogen invasion, phagocytes like macrophages act as the first line of defense, presenting antigens to T-cells and B-cells as antigen-presenting cells (APCs). Helper T-cells (Th) activate B-cells and modulate immune responses, while Killer T-cells (Tk) inhibit responses to maintain stability. The immune response stabilizes when antigen and antibody levels are minimal.

B. Adaptive Model Free Deadbeat Predictive Current Control With Immune Algorithm

The IA has been extensively utilized to tackle a wide range of optimization challenges, drawing inspiration from the operational mechanisms of the humoral immune system. IA's proficiency in parameter optimization provides an efficient means of tackling optimization challenges. Based on the above analysis, Table I illustrates the correlation between the biological immune system and the IA.

Based on Table I, the corresponding mathematical expressions for immune cells are redesigned. First, let the number of the

TABLE I
RELATIONSHIP BETWEEN BIOLOGICAL IMMUNE SYSTEM AND IMMUNE ALGORITHM

Biological immune system	Immune algorithm
Antibody	Error detection
Antigen	Input error
Recognition of Antigen	optimum solution
Tc inhibition	Eliminate the remaining solution
B-cell stimulation	Desired output

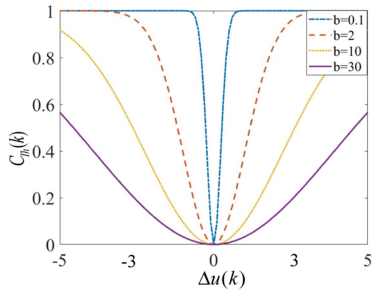

Fig. 6. Curves of $g(\Delta u)$ when parameter b changes.

kth antigen be denoted as e(k), and the antigens stimulate and produce Th cells, and the Th cells concentration is represented by $C_{Th}(k)$. Tk cells concentration is represented by $C_{Tk}(k)$, which is used to inhibit Th cells. The concentration of antibody, produced by B cells, is influenced by Th cells and Ts cells, which is shown as

$$u(k) = C_{Th}(k) - C_{Tk}(k) \tag{23}$$

$$C_{Th}(k) = m_1 e(k) \tag{24}$$

$$C_{Tk}(k) = m_2 g[\Delta u(k)] e(k) \tag{25}$$

where $u(k)$ is the concentration of antibody, m_1 and m_2 are the stimulatory factors of the Th cells and Tk cells. $g(\Delta u(k)) = 1 - \exp(-\Delta u(k)^2/b)$ and it is a nonlinear function that is related to the density of antigens. b is an adjustable parameter that determines the input/output relationship and shapes the nonlinear function $g(\Delta u)$ curve, ensuring that the condition $0<g(\Delta u)<1$ always be satisfied. Fig. 6 shows the $g(\Delta u)$ curves as the parameter b changes, and it is evident that as the parameter b increases, the $g(\Delta u)$ curves will become smoother.

Based on (23), (24), and (25), the concentration of the antibody can be derived as

$$u(k) = m_1 e(k) - m_2 g[\Delta u(k)] e(k) = k_s e(k). \tag{26}$$

For the IA, the key point lies in adaptively adjusting the antibody concentration according to (26), where k_s is the key regulatory factor and it can be derived as

$$k_s = m_1 \left[1 - \mu \left(1 - \exp\left(\frac{-\Delta u(k)^2}{b}\right)\right)\right] \tag{27}$$

where $\mu = m_2/m_1$.

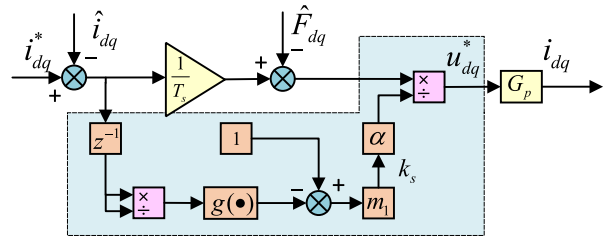

Fig. 7. Block diagram of an immune feedback control.

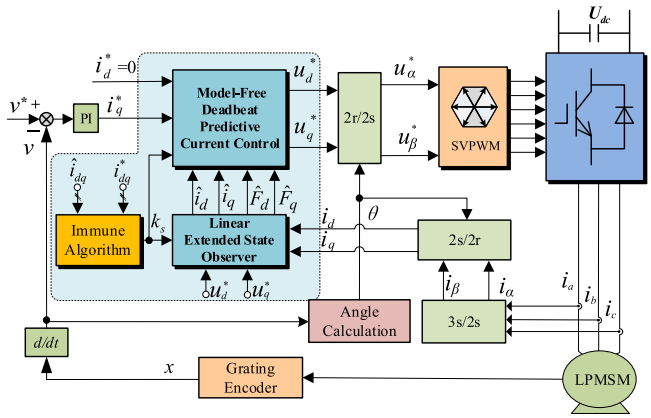

Fig. 8. Block diagram of the LPMSM drive system based on the proposed AMFDPCC-IA.

For the IA introduced into MFDPCC, the construction of a similar regulatory factor k_s can be inspired by the adaptive regulation of antibody concentration, thereby regulating the gain α.

In this article, the IA is integrated with MFDPCC to enhance the dynamic response and steady-state performance of the system. The differential value between the predicted current $\hat{i}_{dq}(k+1)$ and the reference current $i_{dq}^*(k)$ is taken as the input, which is expressed as $\Delta u(k)$ in (27). On the basis of regulatory factor k_s obtained by (26), the gain α in the controller is replaced by $k_s\alpha$. The block diagram of an immune feedback control is shown in Fig. 7, in which the highlighted section can be divided into three main parts: the first part involves the calculation of k_s using (27). Then, k_s is multiplied with the gain α. Finally, the desired dq-axis voltage values are calculated based on (13).

Fig. 8 shows the block diagram of the LPMSM drive system utilizing the proposed AMFDPCC-IA, in which the fixed gain α in MFDPCC controller is dynamically adjusted based on the IA, leading to an improved balance between the system's dynamic and steady-state performance.

C. Reference Voltage Calculation

Combining the IA with the ultralocal model, the improved ultralocal model can be expressed as

$$\dot{y} = k_s \alpha u + F. \tag{28}$$

Based on (27), the regulatory factor k_s can be obtained, then the fixed gain α in (8) is replaced by $k_s\alpha$.

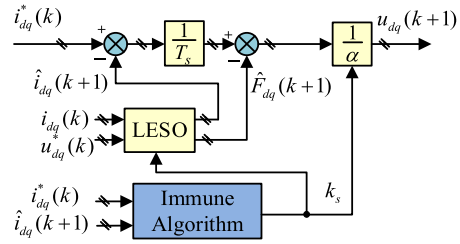

Fig. 9. Block diagram of the AMFDPCC-IA.

TABLE II
PARAMETERS OF THE TESTED LPMSM

Parameter (Unit)	Value
Peak thrust (N)	268
Rated thrust (N)	98
Mover mass (Kg)	0.7
Pole pitch (mm)	30
Stator inductance (mH)	37.1
Stator resistance (Ω)	8.4

Based on (13) and (28), the expression of the voltage reference can be rewritten as

$$u^*_{dq}(k+1)=\frac{-\hat{F}_{dq}(k+1)T_s+i^*_{dq}(k+2)-\hat{i}_{dq}(k+1)}{k_s\alpha_{dq}T_s} \tag{29}$$

where $\hat{i}_{dq}(k+1)$, $\hat{F}_{dq}(k+1)$ are still estimated by LESO. The reference currents $i^*_d(k+2)$ and $i^*_q(k+2)$ can be assumed to remain nearly unchanged between two sampling intervals, provided that the sampling time is sufficiently short, which can be described as: $i^*_d(k+2)=i^*_d(k)$, $i^*_q(k+2)=i^*_q(k)$. Since the calculation of the reference voltage is dynamically regulated by the IA, the estimation of $\hat{i}_{dq}(k+1)$ and $\hat{F}_{dq}(k+1)$ should also be dynamically regulated by the IA, which can be shown as

$$\begin{cases} e_{dq}(k)=\hat{i}_{dq}(k)-i_{dq}(k) \\ \hat{i}_{dq}(k+1)=\hat{i}_{dq}(k)+T_s\left(\hat{F}_{dq}(k)+k_s\alpha u_s(k)\right. \\ \qquad\qquad \left.-T_s\beta_1 e_{dq}(k)\right) \\ \hat{F}_{dq}(k+1)=\hat{F}_{dq}(k)-T_s\beta_2 e_{dq}(k) \end{cases}. \tag{30}$$

The structure of the AMFDPCC-IA is shown in Fig. 9, in which the IA is used to adjust the parameters dynamically to enhance the steady-state and dynamic performance of the system.

The flow diagram of the proposed AMFDPCC-IA is introduced in Fig. 10, and the specific execution process is as follows.

Execution of the proposed AMFDPCC-IA.

1. Initialize the system.
2. Measure velocity v and current i_{dq}.
3. Calculate predicted current $\hat{i}_{dq}(k+1)$ and disturbance values of $\hat{F}_{dq}(k+1)$.
4. According to the differential value between the predicted current $\hat{i}_{dq}(k+1)$ and the reference current $i_{dq}{}^*$, calculate the gain coefficient k_s by immune algorithm.
5. Calculate the reference voltage $u_{dq}{}^*$.
6. The calculated vector voltage is delivered to the motor through the inverter.

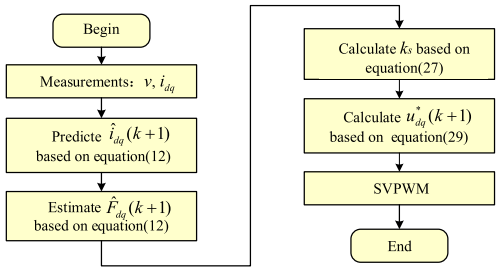

Fig. 10. Flow diagram of AMFDPCC-IA.

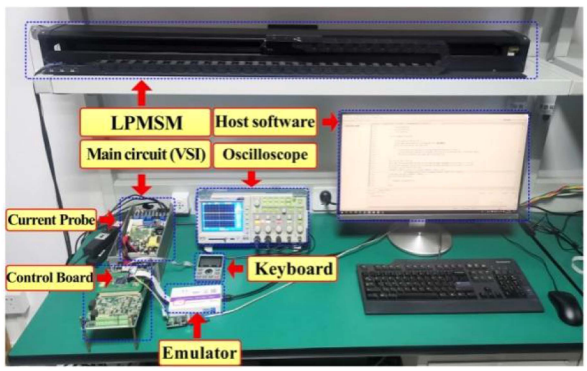

Fig. 11. Experimental platform.

V. EXPERIMENTAL RESULTS

A. Experimental Platform

To validate the correctness and effectiveness of the proposed AMFDPCC-IA, the experiments are carried out on a 0.9-kW LPMSM drive system. The experimental platform is shown in Fig. 11, in which the parameters of the tested LPMSM is shown in Table II. The TMS320F28335 DSP is chosen as the main control chip for the drive system. In the speed control loop, the coefficients of the PI controller are set to $k_p=15$ and $k_i=20$, respectively. For the IA, the parameters are set based on the principle of adjusting the antibody concentration to enhance the immune capability, which are $m_1=1$, $b=0.4$ and $\mu=0.04$, respectively. For LESO, the bandwidth ω_0 is set to 100 rad/s.

B. α Adaptive Performance Verification

To assess the adaptive performance of the ultralocal model gain α under various conditions, different values are set to α, and the associated experimental results are illustrated in Figs. 12–14. The experimental waveforms include the gain α, the q-axis stator current i_q, the velocity v, and the a-axis current i_a.

As depicted in Fig. 12, the experimental results highlight the start-up response, underscoring the impact of α on the system's initial performance. It can be observed that under the same command velocity of 0.1 m·s^{-1}, the start-up time is about 61 ms when the value of α is 10. As α increases from

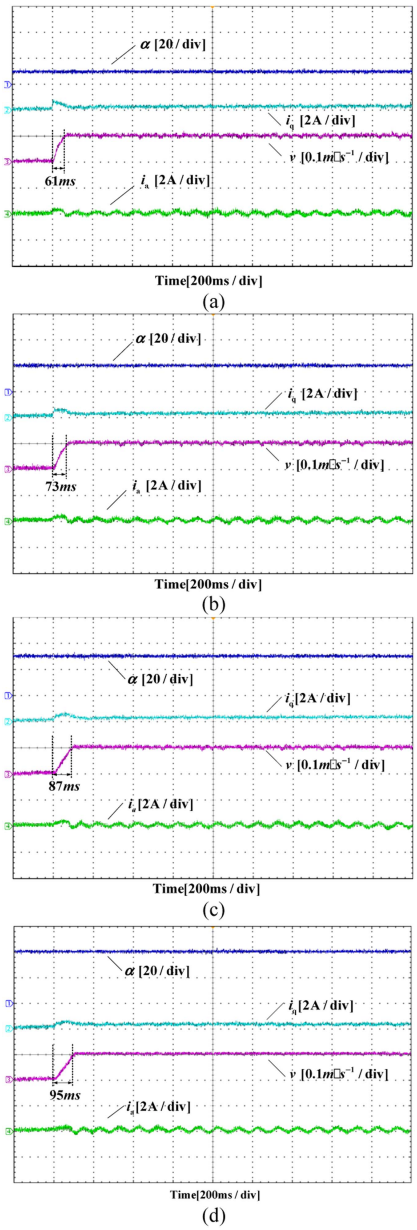

Fig. 12. Experimental results of the start-up responses under different α values. (a) $\alpha = 10$. (b) $\alpha = 20$. (c) $\alpha = 30$. (d) $\alpha = 40$.

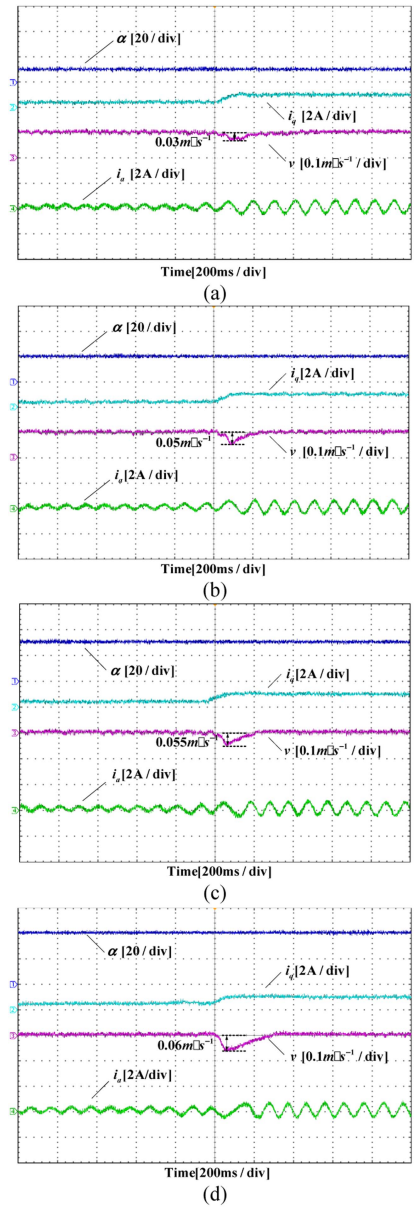

Fig. 13. Experimental results of the step load responses under different α values. (a) $\alpha = 10$. (b) $\alpha = 20$. (c) $\alpha = 30$. (d) $\alpha = 40$.

10 to 40, the rising time increases accordingly, i.e., the rising time are 73 ms, 87, and 95 ms when the values of α are 20, 30 and 40, respectively. Meanwhile, it also can be observed that as α increases, the current torque ripple decreases and the steady-state performance improves. The experimental results indicate that as α increases, the dynamic response time is getting longer, however, the steady-state performance is getting better. There is a trade-off between dynamic response and steady-state performance.

Fig. 13 shows the step load response when the LPMSM is running stably at 0.1 m·s^{-1}. It can be seen from the figure that the velocity drop increases with the increase of α values. When the values of α are 10, 20, 30 and 40, the corresponded velocity drops are 0.03 m·s^{-1}, 0.05 m·s^{-1}, 0.055 m·s^{-1} and 0.06 m·s^{-1}, respectively. By comparing the Fig. 13(a) to Fig. 13(d), it is evident that as α increases continuously, the load capacity of the motor continues to decline.

Fig. 14 shows the experimental results when α changes suddenly, in which α in Fig. 14(a) changes from 20 to 40, and α in Fig. (b) changes from 20 to 10. In Fig. 14(a) and (b), by comparing the velocity and the q-axis current before and after α changes, it can be observed that as α increases, both the velocity fluctuation and current fluctuation decrease. From the perspective of improving the steady-state performance of the drive system, a larger α value leads to the better performance.

From Figs. 12 to 14, it can be observed that the drive system exhibits better dynamic performance with a smaller value of α, however, a larger value of α is conducive for improving the steady-state performance. There exists a dilemma between

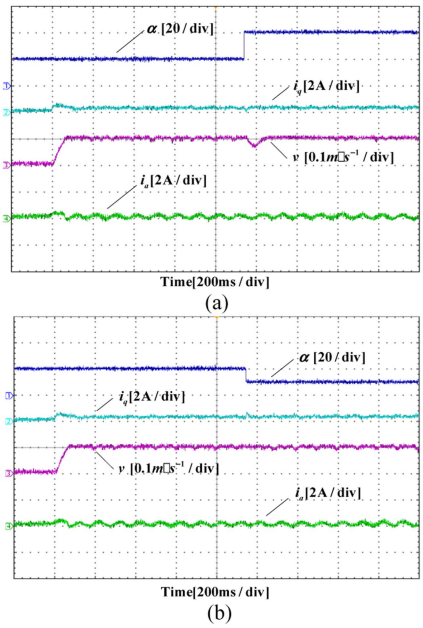

Fig. 14. Experimental results when the value of α suddenly changes. (a) α suddenly changes from 20 to 40. (b) α suddenly changes from 20 to 10.

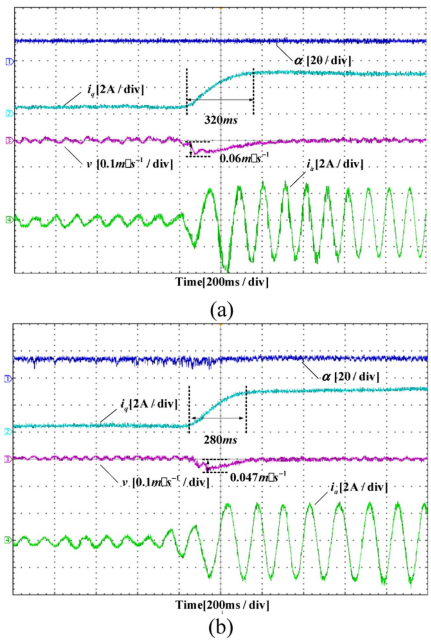

Fig. 15. Experimental results with a step rated load at 0.1 m·s^{-1}. (a) MFDPCC. (b) AMFDPCC-IA.

dynamic response and steady-state performance. To achieve the balance between the dynamic and steady-state performance, the value of α is set to 15 in this article after the tedious debugging process. In the subsequent experimental results, the value of α in the conventional MFDPCC is set to 15. The corresponding experimental result is the AMFDPSC-IA proposed in this article, in which the value of α is dynamically adjusted by the IA.

C. Comparative Test

Fig. 15 shows experimental results of the step rated load response when the motor operates at 0.1 m·s^{-1}. It can be observed that when the rated load is suddenly added, the current response time of the conventional MFDPCC and the proposed AMFDPCC-IA are 320 and 280 ms, respectively. The current response time is shortened by 12.5% due to the dynamic regulation of IA. Meanwhile, the velocity drops of the conventional MFDPCC and the proposed AMFDPCC-IA are 0.06 m·s^{-1} and 0.047 m·s^{-1}, respectively. The velocity drop is reduced by about 21.6% because of the dynamical adjustment by IA. It can be concluded that the proposed AMFDPCC-IA shows better load capacity compared to conventional MFDPCC.

Fig. 16 shows the experimental results when the motor is running in the reciprocating motion process, in which the command velocity is set as 0.05 m·s^{-1}. It can be seen that the current fluctuations of the conventional MFDPCC and the proposed AMFDPSC-IA are 0.5 and 0.4 A, respectively, which means that with the dynamical regulation by the IA, the current fluctuation is reduced by about 20%. Meanwhile, the velocity fluctuations of the conventional MFDPCC and the proposed AMFDPSC-IA are 0.02 m·s^{-1} and 0.015 m·s^{-1}, respectively, which means that with the dynamical adjustment by the IA, the velocity fluctuation is reduced by about 25%. By comparing Fig. 16(a) and (b), it

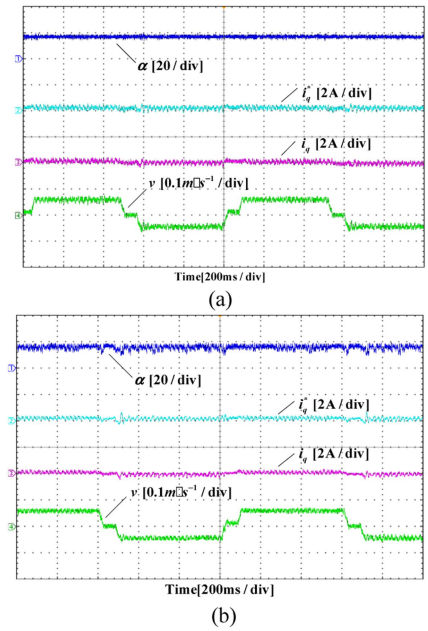

Fig. 16. Experimental results under reciprocating motion. (a) MFDPCC. (b) AMFDPCC-IA.

can be concluded that during the reciprocating motion process, the IA continuously and dynamically adjusts the gain α, thereby the performance of the system has been enhanced.

To validate the robustness of the proposed AMFDPCC-IA, the inductance variation test is chosen as the typical circumstance since the inductance shows the most significant influence on the control performance based on the ultralocal model structure. The comparative experimental results are verified in Fig. 17, in which the inductance L_s is changing from the nominal value to

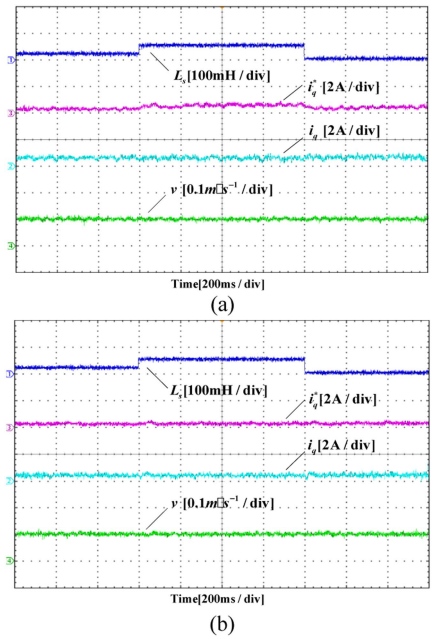

Fig. 17. Experimental results under L_s mismatch. (a) MFDPCC. (b) AMFDPCC-IA.

50% and 200% of the nominal value. It can be seen that when the inductance mismatch occurs, the proposed AMFDPCC-IA has the smaller current fluctuation and velocity fluctuation than that of conventional MFDPCC. According to the figure, the proposed AMFDPCC-IA demonstrates a 17% reduction in current error when compared with the conventional MFDPCC. Therefore, it can be concluded that when motor inductance mismatch occurs, the proposed AMFDPCC-IA shows the better robust performance.

Through the experimental results, it can be clearly observed that compared with the traditional MFDPCC, the introduction of the IA enables the gain α to be adaptively adjusted, which improves the dynamic and steady-state performance of the system. Meanwhile, the increased computational complexity is relatively low and tolerable.

VI. Conclusion

In this article, an AMFDPCC-IA is proposed to enhance the system performance. First, the impact of parameters mismatch on traditional DPCC is analyzed, and an ultralocal model is then developed to replace the conventional LPMSM model. Since the ultralocal model is built based on the system's input and output, the dependence on the motor parameters can be eliminated largely. The control performance of the ultralocal model with conventional fixed gain is analyzed in detail, and it points out that there exits the contradiction between the dynamic and steady-state performance. Thus, to effectively balance the conflict, the IA is introduced to optimize the fixed parameter adaptively. The experimental results show that the proposed AMFDPCC-IA achieves the better dynamic and steady-state performance than the conventional MFDPCC.

References

[1] L. Wang, J. Zhao, Z. Yu, Z. Pan, and Z. Zheng, "Robust and high-precision position control of PMLSM-driven feed servo system based on adaptive fast nonsingular terminal sliding mode," *IEEE Trans. Transp. Electrific.*, vol. 11, no. 1, pp. 4882–4894, Feb. 2025.

[2] M. Wang, L. Li, and D. Pan, "Detent force compensation for PMLSM systems based on structural design and control method combination," *IEEE Trans. Ind. Electron.*, vol. 62, no. 11, pp. 6845–6854, Nov. 2015.

[3] A. Wang, L. Li, and X. Huang, "Modified robust predictive current control design of windings-discontinuous-segmented PMLSM based on an improved analysis method," *IEEE Trans. Power Electron.*, vol. 40, no. 1, pp. 774–786, Jan. 2025.

[4] K. Kang, M. Wang, J. Sun, C. Zhang, and L. Li, "Nonlinear friction compensation for PMLSM using an enhanced adaptive friction observer," *IEEE Trans. Ind. Electron.*, vol. 71, no. 12, pp. 16234–16244, Dec. 2024.

[5] G. Zhang et al., "PR internal mode extended state observer-based iterative learning control for thrust ripple suppression of PMLSM drives," *IEEE Trans. Power Electron.*, vol. 39, no. 8, pp. 10095–10105, Aug. 2024.

[6] X. Wu, J. Kang, M. Yang, T. Wu, and S. Huang, "Robust deadbeat predictive current control for SPMSM using parameter adaptive incremental model," *IEEE Trans. Transp. Electrific.*, vol. 11, no. 1, pp. 4609–4618, Feb. 2025.

[7] Y. Wang et al., "A robust DPCC for IPMSM based on a full parameter identification method," *IEEE Trans. Ind. Electron.*, vol. vol. 70, no. 8, pp. 7695–7705, Aug. 2023.

[8] M. Tian, B. Wang, Y. Yu, Q. Dong, and D. Xu, "Static-errorless deadbeat predictive current control for PMSM current harmonics suppression based on vector resonant controller," *IEEE Trans. Power Electron.*, vol. 38, no. 4, pp. 4585–4595, Apr. 2023.

[9] C. Xie, S. Zhang, X. Li, Y. Zhou, and Y. Dong, "Parameter identification for SPMSM with deadbeat predictive current control using online PSO," *IEEE Trans. Transp. Electrific.*, vol. 10, no. 2, pp. 4055–4064, Jun. 2024.

[10] B. Wang et al., "Static-errorless deadbeat predictive current control using second-order sliding-mode disturbance observer for induction machine drives," *IEEE Trans. Power Electron.*, vol. 33, no. 3, pp. 2395–2403, Mar. 2018.

[11] X. Wu, J. Kang, M. Yang, T. Wu, and S. Huang, "Model-free deadbeat predictive current control for SPMSM based on adaptive gain extended state observer," *IEEE Trans. Transp. Electrific.*, vol. 11, no. 1, pp. 4618–4609, Feb. 2025.

[12] C. Lai, G. Feng, K. Mukherjee, J. Tjong, and N. C. Kar, "Maximum torque per ampere control for IPMSM using gradient descent algorithm based on measured speed harmonics," *IEEE Trans. Ind. Inform.*, vol. 14, no. 4, pp. 1424–1435, Apr. 2018.

[13] Y. Zhou, S. Zhang, C. Zhang, X. Li, X. Li, and X. Yuan, "Current prediction error based parameter identification method for SPMSM with deadbeat predictive current control," *IEEE Trans. Energy Convers.*, vol. 36, no. 3, pp. 1700–1710, Sep. 2021.

[14] P. Cao, X. Zhang, and S. Yang, "A unified-model-based analysis of MRAS for online rotor time constant estimation in an induction motor drive," *IEEE Trans. Ind. Electron.*, vol. 64, no. 6, pp. 4361–4371, Jun. 2017.

[15] L. Wang, S. Zhang, C. Zhang, and Y. Zhou, "An improved deadbeat predictive current control based on parameter identification for PMSM," *IEEE Trans. Transp. Electrific.*, vol. 10, no. 2, pp. 2740–2753, Jun. 2024.

[16] Q. Wang, G. Wang, N. Zhao, G. Zhang, Q. Cui, and D. Xu, "An impedance model-based multiparameter identification method of PMSM for both offline and online conditions," *IEEE Trans. Power Electron.*, vol. 36, no. 1, pp. 727–738, Jan. 2021.

[17] T. Boileau, N. Leboeuf, B. Nahid-Mobarakeh, and F. Meibody-Tabar, "Online identification of PMSM parameters: Parameter identifiability and estimator comparative study," *IEEE Trans. Ind. Appl.*, vol. 47, no. 4, pp. 1944–1957, Jul. 2011.

[18] B. Wang, X. Chen, Y. Yu, G. Wang, and D. Xu, "Robust predictive current control with online disturbance estimation for induction machine drives," *IEEE Trans. Power Electron.*, vol. 32, no. 6, pp. 4663–4674, Jun. 2017.

[19] F. Wang, L. He, J. Kang, R. Kennel, and J. Rodríguez, "Adaptive model predictive current control for PMLSM drive system," *IEEE Trans. Ind. Electron.*, vol. 70, no. 4, pp. 3493–3502, Apr. 2023.

[20] A. Wang, L. Li, and X. Huang, "Improved discrete-time resonant extended state observer based robust DPCC of winding-discontinuous-segmented PMLSM," *IEEE Trans. Ind. Electron.*, vol. 72, no. 6, pp. 5716–5727, Jun. 2025.

[21] J. Lei, S. Fang, D. Huang, and Y. Wang, "Enhanced deadbeat predictive current control for PMSM drives using iterative sliding mode observer," *IEEE Trans. Power Electron.*, vol. 38, no. 11, pp. 13866–13876, Nov. 2023.
[22] J. Chen, Y. Fan, M. Cheng, Q. Zhang, and Q. Chen, "Parameter-free ultralocal model-based deadbeat predictive current control for PMVMs using finite-time gradient method," *IEEE Trans. Ind. Electron.*, vol. 70, no. 6, pp. 5549–5559, Jun. 2023.
[23] N. Yang, S. Zhang, X. Li, and X. Li, "A new model-free deadbeat predictive current control for PMSM using parameter-free Luenberger disturbance observer," *IEEE J. Emerg. Sel. Topics Power Electron.*, vol. 11, no. 1, pp. 407–417, Feb. 2023.
[24] Y. Wang, S. Fang, and D. Huang, "An improved model-free active disturbance rejection deadbeat predictive current control method of PMSM based on data-driven," *IEEE Trans. Power Electron.*, vol. 38, no. 8, pp. 9606–9616, Aug. 2023.
[25] J. Zhao, Y. Zhang, and X. Wang, "Model-free predictive current control of PMSM drives based on variable sequence space vector modulation using an ultra-local model," *IEEE Trans. Transp. Electrific.*, vol. 10, no. 2, pp. 3518–3528, Jun. 2024.
[26] Y. Zhang, J. Jin, and L. Huang, "Model-free predictive current control of PMSM drives based on extended state observer using ultralocal model," *IEEE Trans. Ind. Electron.*, vol. 68, no. 2, pp. 993–1003, Feb. 2021.
[27] F. M. Fayez, M. M. Amin, A. S. Soliman, and O. A. Mohammed, "Optimal adaptive ultra-local model-free control based-extended state observer for PMSM driven single-axis servo mechanism system," *IEEE Trans. Ind. Appl.*, vol. 60, no. 5, pp. 7728–7745, Sep./Oct. 2024.
[28] Y. Wei, H. Young, D. Ke, D. Huang, F. Wang, and J. Rodríguez, "Adaptive ultralocalized time-series for improved model-free predictive current control on PMSM drives," *IEEE Trans. Power Electron.*, vol. 39, no. 5, pp. 5155–5165, May 2024.
[29] Y. Wei, H. Young, D. Ke, F. Wang, H. Qi, and J. Rodríguez, "Model-free predictive control using sinusoidal generalized universal model for PMSM drives," *IEEE Trans. Ind. Electron.*, vol. 71, no. 11, pp. 13720–13731, Nov. 2024.
[30] Q. Zhu, Z. Yin, Y. Zhang, J. Niu, Y. Li, and Y. Zhong, "Research on two-degree-of-freedom internal model control strategy for induction motor based on immune algorithm," *IEEE Trans. Ind. Electron.*, vol. 63, no. 3, pp. 1981–1992, Mar. 2016.
[31] Y. Zhang, S. Li, W. Yi, Y. Yang, K. Cao, and B. Luo, "A robust model predictive current closed-loop control with parameter estimation strategy based on immune chaotic antipredator PSO for PMSM," *IEEE Trans. Power Electron.*, vol. 40, no. 1, pp. 1836–1848, Jan. 2025.
[32] J. Yuan et al., "An immune-algorithm-based dead-time elimination PWM control strategy in a single-phase inverter," *IEEE Trans. Power Electron.*, vol. 30, no. 7, pp. 3964–3975, Jul. 2015.
[33] T. Amraee, A Ranjbar, and R. Feuillet, "Immune-based selection of pilot nodes for secondary voltage control," *Eur. Trans. Elect. Power*, vol. 20, no. 7, pp. 938–951, Jul. 2010.
[34] K. Yu and Z. Wang, "Improved deadbeat predictive current control of dual three-phase variable-flux PMSM drives with composite disturbance observer," *IEEE Trans. Power Electron.*, vol. 37, no. 7, pp. 8310–8321, Jul. 2022.
[35] S. A. Davari, S. Azadi, F. Flores-Bahamonde, F. Wang, P. Wheeler, and J. Rodriguez, "Compensating the measurement error in model-free predictive control of induction motor via Kalman filter-based ultra-local model," *IEEE Trans. Ind. Electron.*, vol. 39, no. 12, pp. 15811–15821, Dec. 2024.

Yanqing Zhang (Member, IEEE) received the B.S., M.S., and Ph.D. degrees in electrical engineering from Xi'an University of Technology, Xi'an, China, in 2012, 2015, and 2019, respectively.

In 2019, he was with the School of Electrical Engineering, Xi'an University of Technology, where he is currently an Associate Professor. His main field of interest is high performance control of ac motor.

Hongtao Yuan was born in Shaanxi, China, in 1996. He received the B.S. degree in electrical engineering in 2022 from Xi'an University of Technology, Xi'an, China, where he is currently working toward the M.S. degree in electrical engineering.

His main research interest includes high performance control of linear permanent magnet synchronous motor.

Zhonggang Yin (Member, IEEE) received the B.S., M.S., and Ph.D. degrees in electrical engineering from Xi'an University of Technology, Xi'an, China, in 2003, 2006, and 2009, respectively.

In 2009, he was with the School of Electrical Engineering, Xi'an University of Technology, where he is currently a Professor. His research interests include high performance control of ac motor and digital control of power converters.

Dr. Yin is currently an Associate Editor for IEEE TRANSACTIONS ON INDUSTRIAL ELECTRONICS.

Cong Bai was born in Shaanxi, China, in 1993. She received the B.S., M.S., and Ph.D. degrees in electrical engineering from Xi'an University of Technology, Shaanxi, China, in 2015, 2019, and 2023, respectively.

In 2023, she was with the School of Electrical Engineering, Xi'an University of Technology, where she is currently an Associate Professor. Her main research interests include high performance control of linear motor and servo motor.